Journal of Applied Polymer Science

# Zinc Sulfide Nanoparticles Template by Bacterial Cellulose and Their Optical Properties

**Weili Zheng, Shiyan Chen, Siyu Zhao, Yi Zheng, Huaping Wang**

State Key Laboratory for Modification of Chemical Fibers and Polymer Materials, Key Laboratory of Textile Science & Technology (Ministry of Education), College of Materials Science and Engineering, Donghua University, Shanghai 201620, People's Republic of China

Correspondence to: S. Chen (E-mail: chensy@dhu.edu.cn) and H. Wang (E-mail: wanghp@dhu.edu.cn)

**ABSTRACT:** Spherical zinc sulfide (ZnS) nanoparticles dispersed on bacterial cellulose (BC) nanofibers homogeneously were successfully fabricated through *in situ* precipitation method using BC as template and explored the formation mechanism. The structure and properties were characterized by Fourier transform infrared, X-ray diffractometer, FESEM, and so on. The results demonstrated that the nanoparticles were sphalerite structure ZnS and the size increased with the increase of the zinc precursor concentrations. Moreover, a high photocatalytic activity (92%) for degradation of methyl orange was observed and the photoluminescence spectra of the nanocomposites exhibited a blue emission band centered at 468 nm. The flexible BC membrane carried of ZnS nanoparticles might be a promising candidate in the application fields of fluorescence and photo-catalysis. © 2014 Wiley Periodicals, Inc. J. Appl. Polym. Sci. **2014**, *131*, 40874.

**KEYWORDS:** application; bacterial cellulose; optical properties; template; zinc sulfide

Received 10 November 2014; accepted 15 April 2014
**DOI: 10.1002/app.40874**

## INTRODUCTION

ZnS quantum dots (QDs) as semiconductor nanocrystals have attracted enormous research interests in recent years. They were remarkably different from their bulk materials due to their unique optical and photochemical properties. Benefit from their quantum confinement effects and large surface area,[1,2] ZnS QDs have been considered to be the promising candidates in the application fields such as fluorescence, sensors, photo-catalysis, and solar cells.[3–6] Moreover, compared with other QDs, the low toxicity makes them suitable for candidates in several biological applications as bioelectronics, bio-analytics, and bio-diagnostics.[7–9] Therefore, the immobilization of the ZnS QDs into a flexible organic matrix through the hybridization with natural polymers like cellulose or cellulose derivatives has been investigated during last decades with potential application in security paper with optical signatures.[10–15]

BC membranes, obtained through fermentation mainly by the Acetobacter xylinum, are generated as an ultrafine nano sized three-dimensional (3D) fibrous network comprised of the ribbon-shaped nanofibers with diameters of 10–100 nm.[16,17] Unlike low-crystalline natural fibers which contains only 55–65% cellulose, high-crystalline BC composed of pure cellulose (free of lignin, pectin, and hemi-cellulose) can be synthesized during the extracellular process, and show excellent mechanical properties of high tensile strength (>2 GPa).[18] In addition, it possesses unique structures of ultrafine 3D network with a distinct tunnel and pore structure and properties such as high water holding capacity and good biocompatibility. Their high specific surface area with plenty of hydroxyl groups and ether group serve as the active site for metal ions absorption. Taking advantage of their unique properties, BC could serve as an excellent template or matrix for *in situ* synthesis nanomaterials with a specific morphology and size.[19–22]

Herein, we first reported an *in situ* homogeneous precipitation for fabricating spherical ZnS nanoparticles template by BC as follows: first, the zinc precursor penetrated into the inner space of BC membranes and were absorbed on the active sites, and then the anchored zinc precursor reacted with the sulfide ions released from the decomposition of thioacetamide. Finally, the spherical ZnS nanoparticles generated through *in situ* crystallization with a uniform distribution on the BC nanofibers.[23,24] The influence of the zinc precursor concentrations on the morphologies and size of ZnS nanoparticles were investigated. The possible growth mechanism for the formation of ZnS nanoparticles on the BC nanofibers was explored and the properties were discussed.

## EXPERIMENTAL

### Materials and Characterization

The purified BC membranes were synthesized in our lab. Tioacetamide (TAA) was purchased from Adamas Reagent.

Analytical zinc acetate dehydrate, acetic acid, sodium hydroxide, and methyl orange were purchased from Sinopharm Chemical Reagent. All chemicals were used as received without any further treatment. High purity water with resistivity of 18.2 MΩ cm was used during the experimental process.

The crystallinity and the phase of the samples were characterized on a X-ray diffractometer (XRD) (D/Max-2550 PC, Rigaku, Japan) with the Cu Ka radiation at a scanning rate of 2°/s ranging from 5° to 60° (2$\theta$ angle). The Fourier transform infrared (FTIR) spectra of the samples were recorded on a Nicolet NEXUS-670 FTIR in the wave number range from 600 to 4000 $cm^{-1}$. The morphologies of the samples were characterized using S-4800 field emission scanning electron micro scope (FESEM). Prior to analysis, the freeze-dried samples were cut into small pieces and coated with gold palladium by cathodic spreading. Thermal gravimetric was performed with a Netzsch TG 209 F1 Iris under nitrogen atmosphere at a heating rate of 20°C/min from room temperature to 800°C. The Brunauer–Emmett–Teller (BET) surface area and pore size distribution of the samples were measured by nitrogen gas absorption (Micromeritics, ASAP 2020 analyzer). Prior to measurements, the samples were degassed at 110°C for 8 h completely. Photoluminescence spectra of the samples were characterized by a JASCO FP-6600 spectrofluorometer. Fluorescence micrographs of the samples excited by ultraviolet light were obtained by Olympus BX51 fluorescence microscope. Tensile strengths of the samples were measured using a WDW 3020 Universal Testing Machine at room temperature with the crosshead speed of 5 mm/min. The freeze-dried samples were cut into 50 mm in length, 20 mm in width, and 0.1 mm in thickness prior to the mechanical measurements.

### Preparation of ZnS/BC Nanocomposites

The BC membranes (4 cm × 5 cm × 1 cm) were pretreated with 1 wt % NaOH solution for 3 h and then were washed sufficiently with pure water until neutral. The purified BC membranes were firstly dipped into 0.1, 0.5, 1, 2.5, and 5 wt % zinc acetate aqueous solution, respectively, with magnetic stirring at room temperature for 12 h to reach the absorption equilibrium of the zinc precursor. Second, TAA were mixed into the system at round-bottomed flasks stirring vigorously, and the system was acidified (pH = 2–2.5) with acetic acid to release the sulfide anions by the decomposition of TAA. The molar ratio of zinc acetate and TAA was controlled as 1 : 4. Subsequently, the system was heated up to 80°C with oil bath for 3 h. Nitrogen was bubbled through the experiments to prevent ZnS nanoparticles on BC nanofibers from oxidation. After that, the ZnS/BC nanocomposite membranes were taken out from the reaction solution and rinsed with pure water several times to remove any loosely anchored zinc sulfide nanoparticles and residual chemical reagents. Finally, the nanocompostites were freeze-dried for the further characterization.

### Measurement of Photocatalytic Activity

The photocatalytic activities of the ZnS/BC nanocomposites were evaluated by the photocatalytic degradation of methyl orange (MO) solutions.[25,26] The measurement procedure can be described as follows: 2 g freeze-dried ZnS/BC nanocomposites were cut into small pieces, added into 100 mL of MO solutions with the concentration of 10 mg/L, and magnetically stirred in the dark for 1 h to reach the absorption equilibrium of MO molecules with the catalysts. Then the reaction solutions were irradiated to UV light at a wavelength of 254 nm. Ten milliliters of the reaction solution was withdrawn at different irradiation time intervals for determining the absorption value ($A_t$) of the solution using a UV–vis spectrophotometer (UV-1200, Shanghai Mapada Instruments). The absorption value ($A_t$) of MO at 460 nm was chosen as the monitored parameter (the maximum absorption wavelength of MO). The degradation efficiency ($D_t$) of MO solution was calculated as eq. (1):

$$D_t(\%) = \frac{A_0 - A_t}{A_0} \times 100\%, \quad (1)$$

where $A_0$ and $A_t$ indicated the absorption value of 10 mg/L MO solution and the samples at different irradiation time, respectively. The photocatalytic activities of different samples were evaluated by the variation of $D_t$ with the reaction time ($t$). For a further blank experiment to investigate the photocatalytic activities, the solutions of MO were subjected to another two experimental conditions: (1) pure BC membranes under exposure to UV light, (2) 1 wt %-ZnS/BC composites in the dark.

## RESULTS AND DISCUSSION

### Formation of ZnS Nanoparticles on BC

The schematic illustration of ZnS nanoparticles depositing on BC nanofibers is shown in Figure 1. The *in situ* crystallization of ZnS nanoparticles on BC nanofibers can be considered as two steps as follows: (i) absorption of zinc precursor on BC nanofibers, (ii) nucleation and growth. First, when BC membranes immersed in the zinc acetate aqueous solution, $Zn^{2+}$ and $Zn[CH_3COOH]^+$, the dominant zinc precursor in zinc acetate aqueous solution (pH = 6.0–6.5), penetrated into the 3D network of the nanoporous BC membranes. Then the zinc precursor anchor on the active sites of the BC membranes through electrostatic interactions between zinc precursor and hydroxyl groups with lone pair of electrons that can bind zinc precursor through the electron pair sharing.[25] Second, the sulfide anions generate by the thermal decomposition of TAA under acidic pH condition.[27] When the system of the relative supersaturation exceeds the critical supersaturation, the nucleus of ZnS form on the active sites of BC nanofibers immediately and begins to grow through the *in situ* crystallization. According to the report by Robert et al., the size of the synthesized ZnS nanoparticles depend on the pH of the reaction.[24] For pH < 2.5, the $Zn^{2+}$ divalent cations can be fully captured by acetate ligands due to the strong interaction between $Zn^{2+}$ and acetate ligands resulting in the formation of triacetate complexes as the dominant intermediate species during the *in situ* crystallization process of the system and the precipitation kinetics is strongly affected by the presence of such complexes resulting in the formation of nanosized ZnS crystals on the absorbed sites. Herein, the reaction of system is conducted at pH = 2–2.5 to accelerate the decomposition of TAA. During the *in situ* homogeneous precipitation, the size of the newborn nuclei is mainly influenced by the temperature. Sulfide ions concentration is the key to control the growth of the newborn ZnS nucleus during the *in situ*

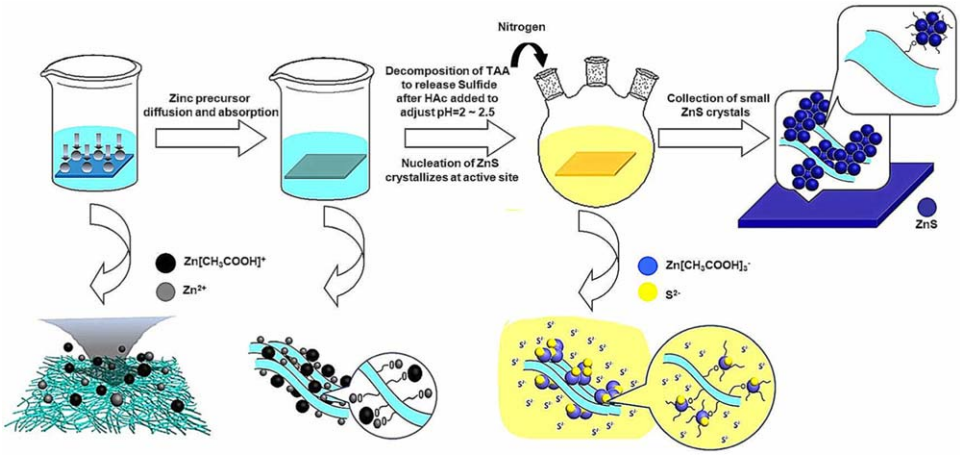


**Figure 1.** Schematic diagram of the formation of ZnS/BC nanocomposite. [Color figure can be viewed in the online issue, which is available at wileyonlinelibrary.com.]

crystallization process due to its low generation rate at low pH of the system and the slow diffusion rate, which results in the delay of growth of nucleus.[23] Meanwhile, the pH of the system about (2–2.5) is relatively close to isoelectric point of ZnS, therefore, the small ZnS crystals have a tendency to diffuse and deposit on the nucleus absorbed on BC nanofibers.[24] The formation and growth of spherical ZnS nanoparticles happen through collection of small newborn crystals instead of the fast growth of the nucleus absorbed on BC. BC guarantee the uniform distribution of ZnS nanoparticles and prevent the ZnS nanoparticles from interparticle aggregation on the nanofibers. Moreover, the rate of sulfide ion generation increases with reaction concentration resulting in the formation of larger ZnS nanoparticles,[27] which is precisely consistent with the XRD and FESEM analyses.

### XRD Analyses

The crystallographic structures of the nanoparticles anchored on BC membranes were investigated by XRD. The XRD patterns of the ZnS/BC nanocomposites synthesized at different zinc precursor concentrations are depicted in Figure 2. The obvious diffraction peaks at 14.6°, 16.7°, and 22.8° in the ZnS/BC nanocomposites shown in Figure 2(a) are assigned to the crystallographic plane of (10), (110), and (200) reflection of BC.[28] The other four major broad peaks at 28.6°, 33.3°, 47.6°, and 56.4° are attributed to the (111), (200), (220), and (311) crystal planes of sphalerite structure of ZnS, respectively.[3] With the rising of zinc precursor concentrations, the intensity of the diffraction peaks increases. This is possibly because more amount of zinc precursor added into the system resulted in the higher crystallinity degree and larger amount of ZnS nanoparticles. The estimated crystal size of the ZnS crystallites in (111) crystal plane of 0.1, 0.5, 1, 2.5, and 5 wt % are 8.9, 11.5, 13.2, 14.1, and 17.3 nm, respectively.[25] As observed, the size of the ZnS crystallites becomes larger with the increasing zinc precursor concentrations.

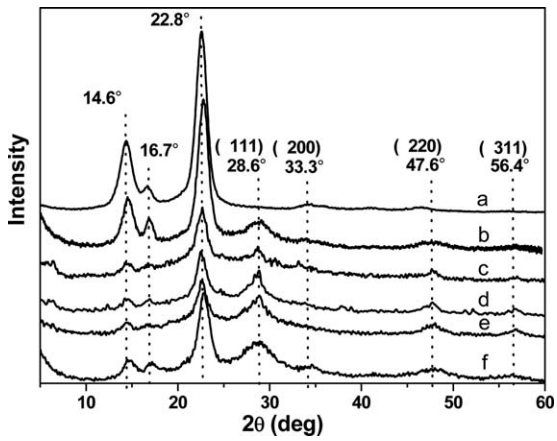


**Figure 2.** XRD patterns of the pure BC membrane (a) and ZnS/BC nanocomposites synthesized at different zinc precursor concentrations: (b) 0.1 wt %, (c) 0.5 wt %, (d) 1 wt %, (e) 2.5 wt %, and (f) 5 wt %.

### FTIR Analysis

FTIR measurements were conducted to discuss the interactions between the ZnS nanoparticles and the BC matrix. The characteristic bands at 3410, 2890, 1640, and 1060 $cm^{-1}$ in Figure 3(a) are attributed to the native BC. The strong band at 3410 $cm^{-1}$ arises from the stretching vibrations of hydroxyl groups. The bands at 2890 and 1640 $cm^{-1}$ are assigned to the C—H stretching and the H—O—H bending vibrations of the absorbed water. A strong band at 1060 $cm^{-1}$ originates from the C—O—C pyranose ring skeletal vibration.[25] Figure 3(b) shows the spectra of the ZnS/BC nanocomposites. We could observe the peaks at 3410 $cm^{-1}$ corresponding to stretching vibrations of hydroxyl groups of BC shifted remarkably to lower wavenumbers (3340 $cm^{-1}$), which proves that the ZnS nanoparticles anchored on the BC have strong interactions with the hydroxyl groups of BC nanofibers.[16] Moreover, the two peaks at 1426 and 1560 $cm^{-1}$ in Figure 3(b) can be attributed to the C—O—M bonds.[23] The presence of C—O—M bonds in the FTIR spectra probably originates from the unreacted acetate–Zn complexes absorbed on the particles, or from the absorption of acetate on the surface of the ZnS nanoparticles.[24]

### Morphological Analysis

The size and distribution of ZnS nanoparticles are greatly influenced by the reaction conditions during the *in situ* crystallization process in homogeneous solution. Herein, we investigated

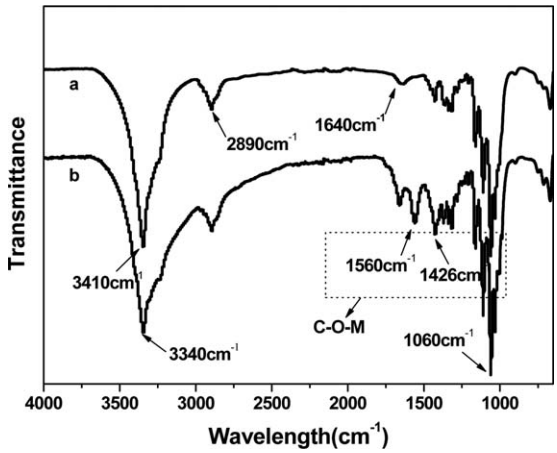


**Figure 3.** The FTIR spectra of the pure BC (a) and ZnS/BC nanocomposite (1 wt %) (b).

the effect of zinc precursor concentrations on the morphologies of ZnS nanoparticles anchored on BC nanofibers. The morphologies of the pure BC and the ZnS/BC nanocomposites are shown in Figure 4. As seen from Figure 4(a), BC nanofibers with the diameters about 70 nm are randomly arranged to form the exquisite 3D network. The nonporous structures of BC membranes performed as the nanoreactor for *in situ* crystallization, which provides a great deal of tunnels for the absorption of zinc precursor and resulted in the homogeneous distribution of zinc precursor on BC nanofibers. Figure 4(b–f) shows the FESEM images of the ZnS nanoparticles synthesized template by BC under different zinc precursor concentrations from 0.1 to 5 wt %. The zinc precursor concentrations have the significant impact on the determination about the size and distribution of ZnS nanoparticle. When the zinc precursor concentrations range from 0.1 to 1 wt %, the average diameters of the nanoparticles on BC are approximately 30, 50, and 100 nm, respectively. And

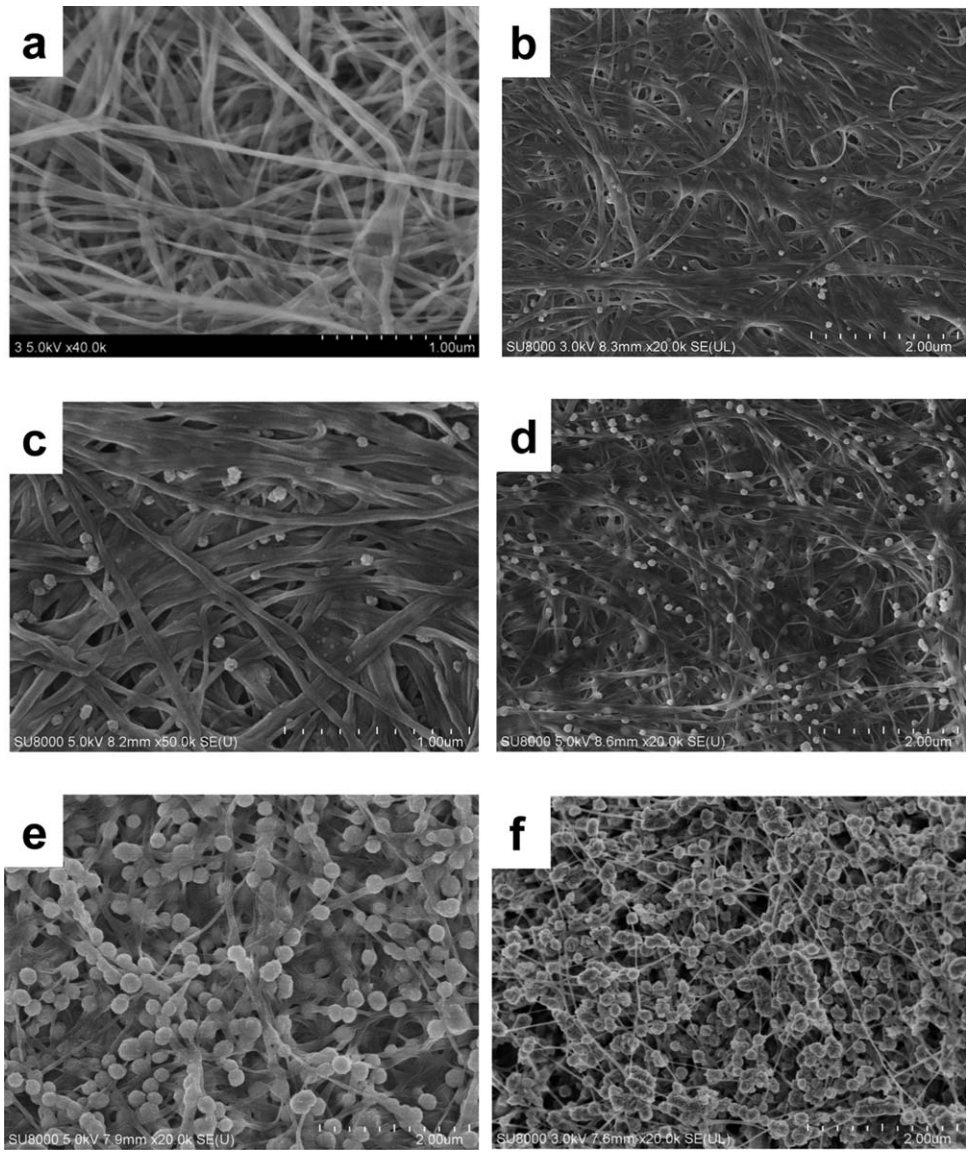


**Figure 4.** FESEM images of the pure BC membrane (a) and ZnS/BC nanocomposites synthesized at different zinc precursor concentrations: (b) 0.1 wt %, (c) 0.5 wt %, (d) 1 wt %, (e) 2.5 wt %, and (f) 5 wt %.

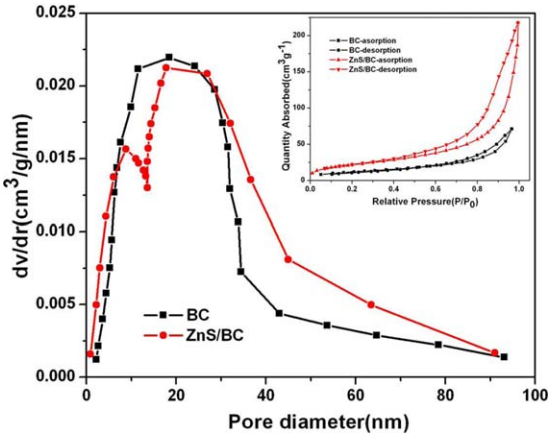


**Figure 5.** The BJH pore size distribution of freeze-dried pure BC and ZnS/BC nanocomposite (1 wt %). Inset shows the nitrogen absorption-desorption isotherms of the freeze-dried pure BC and ZnS/BC nanocomposite (1 wt %). [Color figure can be viewed in the online issue, which is available at wileyonlinelibrary.com.]

it is clearly observed that the quantity of the particles increased with the concentrations. It can be explained that a larger amount of zinc precursor anchor on active sites on BC nanofibers, and form more ZnS nucleus during the *in situ* crystallization resulting in more uniform spherical ZnS nanoparticles discretely onto the BC nanofibers with the increasing zinc precursor concentration. However, when the zinc precursor concentrations increase to 2.5–5 wt %, the unstable ZnS nanoparticles along the BC nanofibers have a tendency to agglomerate with each other forming the irregular aggregates. The average diameters of the nanoparticles grow to about 150–200 nm. Furthermore, compared the estimated average grain size of ZnS nanoparticles with that from XRD analysis, we can clearly find out that the average grain size of ZnS nanoparticles is much smaller than those from the FESEM. That is because the spherical ZnS nanoparticles observed from FESEM exist as polycrystalline structures comprised of many small ZnS single crystals.

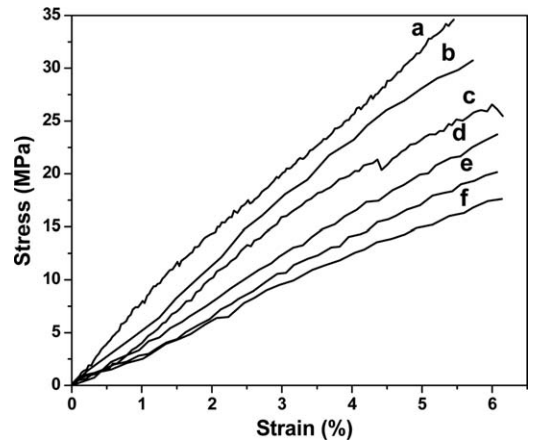


**Figure 6.** Tensile stress–strain behaviors of the pure BC membrane (a) and ZnS/BC nanocomposites synthesized at different concentrations of zinc precursor: (b) 0.1 wt %, (c) 0.5 wt %, (d) 1 wt %, (e) 2.5 wt %, and (f) 5 wt %.

### BET and Porosity Characterization

BET gas sorptometry measurements were conducted to examine the porous structures of the pure BC and ZnS/BC nanocomposite (1 wt %). The Barret–Joyner–Halenda (BJH) pore size distribution and the nitrogen absorption–desorption isotherms of the freeze-dried pure BC and ZnS/BC nanocomposite are presented in Figure 5. It is observed from Figure 5 that pure BC and ZnS/BC nanocomposite are basically mesoporous with a wide pore size distribution predominantly less than 95 nm. Another pore-size distribution around 10 nm (about 8.5 nm) indicates a number of pores presumably arising from the spaces within the ZnS nanoparticles on BC nanofibers, which certifies the nanoporous structure of ZnS nanoparticles generated from the agglomeration of small crystallites. The inset of Figure 5 shows the much higher absorbed nitrogen quantity of the nanocomposite compared with that of the pure BC membranes. And a larger hysteresis loop with the loading of nanoporous structure of ZnS nanoparticles could be observed due to the capillary condensation effect at relative pressure ($P/P_0$) from 0.4 to 1.0, which indicates an increase in the surface area and the total pore volume.[25] BET-specific surface areas of the pure BC and ZnS/BC nanocomposite are measured to be 48.1 and 90.8 $m^2/g$, respectively.

### Mechanical Properties

The mechanical properties of ZnS/BC nanocomposites were investigated by the tensile test. The tensile stress–strain behaviors of the pure BC membranes and ZnS/BC nanocomposites synthesized at different zinc precursor concentrations are depicted in Figure 6 and the tensile strength, elongation, and Young's modulus of nanocomposites calculated according to the stress–strain curves are listed in Table I. It can be found that the Young's modulus and tensile strength of ZnS/BC nanocomposites are lower than the values of Young's modulus (635.2 MPa) and tensile strength (34.6 MPa) of the pure BC due to the loading of nanoparticle. The nanoparticles diminish the strong intramolecular and intermolecular hydrogen bond of BC matrix and led to the stress concentration points owing to the internal cracks of the nanoparticles.[29] All these factors result in the reduction on the mechanical properties of the ZnS/BC nanocomposites. Meanwhile, the Young's modulus and tensile strength of ZnS/BC nanocomposites decrease with the rising the zinc precursor concentrations. It is possible that the agglomeration and fragility of ZnS nanoparticles with the increasing in

**Table I.** Tensile Strength, Elongation, and Young's Modulus of Nanocomposites Determined from Strain–Stress Curves

| Sample | Strain (%) | Stress (MPa) | Young's modulus (MPa) |
|---|---|---|---|
| BC | 5.45 | 34.62 | 635.23 |
| 0.1 | 5.72 | 30.73 | 537.24 |
| 0.5 | 6.15 | 25.47 | 414.15 |
| 1 | 6.07 | 23.73 | 390.94 |
| 2.5 | 6.06 | 20.16 | 332.67 |
| 6 | 6.14 | 17.62 | 286.97 |

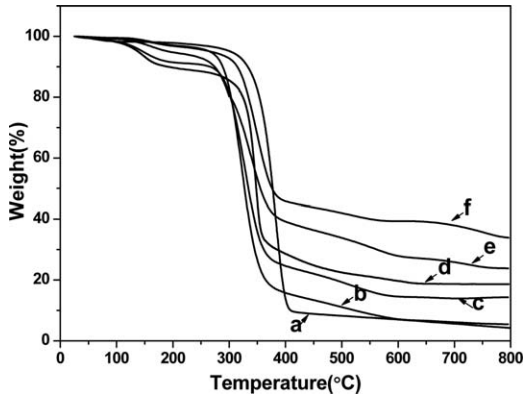


**Figure 7.** TG curves of the pure BC (a) and ZnS/BC nanocomposites synthesized at different zinc precursor concentrations: (b) 0.1 wt %, (c) 0.5 wt %, (d) 1 wt %, (e) 2.5 wt %, and (f) 5 wt %.

the content of the ZnS nanoparticles may result in the decrease of the Young's modulus and tensile strength.

### Thermal Properties

The thermal stability of ZnS/BC nanocomposites were studied by TG measurements. TG curves conducted from room temperature to 800°C of the pure BC and ZnS/BC nanocomposites synthesized at different zinc precursor concentrations are shown in Figure 7. The curve of the pure BC exhibits three significant weight loss platforms. The first weight loss from room temperature to 300°C is due to the dehydration process, in which the absorbed and hydrogen bonded water molecules can be removed absolutely at this stage. The sharp weight loss at the second platform (300–400°C) is caused by the pyrolysis of BC, in which destruction of the crystalline regions of BC and the decomposition of amorphous BC into monomer of D-glucopyranose occur. The weight loss at the third platform (400–600°C) can be attributed to the decarboxylation and decarboxylation reactions forming carbon monoxide and carbon dioxide.[30] The TG curves of ZnS/BC nanocomposites are almost similar to that of pure BC membranes. However, the thermal stability of ZnS/BC nanocomposites deteriorate due to the inclusion of the ZnS nanoparticles into BC matrix, which suggests the existence of the strong interaction between BC membranes and ZnS nanoparticles. The residues of the samples at 800°C are listed in Figure 7 and compared with BC membranes, the difference in residues between the pure BC and nanocomposites could be considered the loading content of ZnS nanoparticles anchored on BC. The corresponding content of ZnS nanoparticles on the nanocomposites is obtained about 1.0, 10.1, 14.4, 19.6, and 29.7 wt % for ZnS/BC nanocomposites synthesized with the zinc precursor concentrations at 0.1, 0.5, 1, 2.5, and 5 wt %, respectively.[25]

### Photocatalytic Properties

ZnS nanomaterials as the semiconductor photocatalyst are widely used for the photocatalytic degradation of organic pollutants such as dyes, *p*-nitrophenol, and halogenated benzene derivatives in wastewater treatment.[5] However, insoluble nanomaterials suspended in the organic solvent incline to aggregate due to the high surface energy in practical application, which will weaken the photocatalytic activities. Otherwise, the separation and recovery of the catalyst require extra costs and inevitably lead to the loss of the catalyst causing secondary pollution. Therefore, template immobilization of nanomaterial technology provides an effective way of suspended catalyst separation and recovery. Meanwhile, the template also could maintain dispersion of nanomaterial to improve the stability of photocatalytic activities. In this article, BC serve as organic template to immobilize ZnS nanoparticles through strong interaction between the hydroxyl groups along BC nanofibers and ZnS nanoparticles. To demonstrate the potential application of the resultant ZnS/BC nanocomposites in this field, the photocatalytic activities of the ZnS/BC nanocomposites were evaluated by the photocatalytic degradation of MO solutions. It is observed that the photocatalytic efficiency of the pure BC membranes under exposure to UV light is almost the same as that of ZnS/BC nanocomposites (1 wt %) without exposure to UV light, where a slight decrease in the concentration of MO can be detected caused by the absorption on the porous nanostructures of the pure BC and ZnS/BC nanocomposites. ZnS nanomaterials display the photocatalytic activity only under high-energy light radiation due to the direct wide band-gap energy (3.66 eV). It is clearly that ZnS/BC (1 wt %) nanocomposites under UV light display a higher photocatalytic activity with a maximum degradation efficiency of 92% at 120 min, and an obvious degradation of MO solutions can be seen from inset picture in Figure 8. The main reason can be attributed to the different specific surface areas and the content of ZnS nanoparticles anchored on BC matrix. The loading content of the ZnS nanoparticles on BC increase with the zinc precursor concentrations from 0.1 to 1 wt % (according to the TG curve in Figure 7 and FESEM images in Figure 4), which indicated a growth on the composited amount of uniform spherical ZnS nanoparticles with similar particle size discretely on the BC membranes. However, when the zinc precursor concentrations reached to 2.5–5 wt %, the agglomeration of ZnS nanoparticles occurred forming the irregular particles, which led to the decrease in the photocatalyst efficiency.

### Photoluminescence Properties

Figure 9 shows the photoluminescence (PL) spectra of the pure BC (a) and ZnS/BC nanocomposites at room temperature with an excitation wavelength at 320 nm. As seen in Figure 9, all

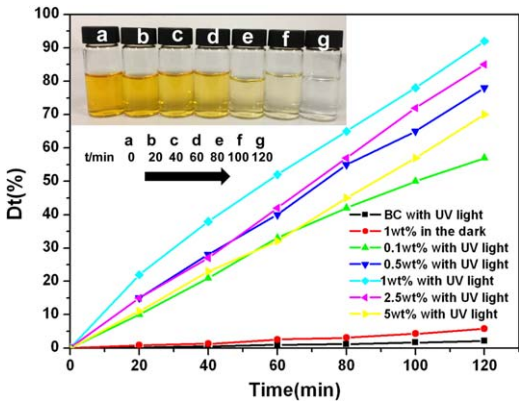


**Figure 8.** Photodegradation of MO (10 mg/L) under different conditions. [Color figure can be viewed in the online issue, which is available at wileyonlinelibrary.com.]

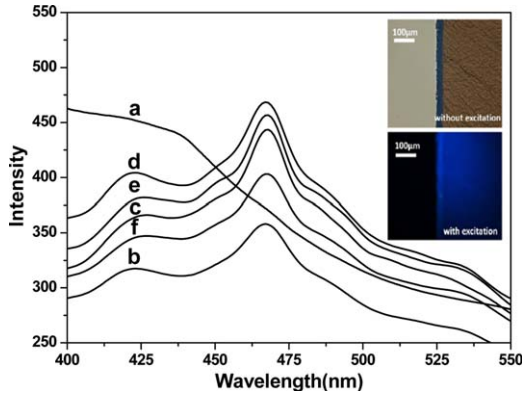


**Figure 9.** PL spectra of the pure BC (a) and ZnS/BC nanocomposites at different zinc precursor concentrations: (b) 0.1 wt %, (c) 0.5 wt %, (d) 1 wt %, (e) 2.5 wt %, and (f) 5 wt %. Inset shows the micrographs of the ZnS/BC nanocomposite (1 wt %) membrane without excitation and with excitation. [Color figure can be viewed in the online issue, which is available at wileyonlinelibrary.com.]

ZnS/BC nanocomposites under UV light excitation display the bimodal distribution with peaks at around 424 nm and 468 nm resulted from the typical defect state. The weak broad peak at 424 nm and a dominant intense blue emission band at 468 nm can be attributed to the emissions due to sulfur vacancies and zinc interstitial defects, respectively.[31,32] A blue-shift about 17 nm to the shorter wavelength emission peaks was observed compared with the bulk ZnS material (the emission of zinc interstitial defects is 485 nm). As been exhibited in PL spectrum, the ZnS/BC nanocomposites (1 wt %) have a stronger PL intensity compared with other nanocomposites synthesized at different concentrations. That is probably because the amount of ZnS nanoparticles (1 wt %) is more than the rest of the samples resulting in the strongest PL emission. This result is well consistent with the morphological analysis. Moreover, an intense blue photoluminescence from the ZnS/BC nanocomposites can be clearly observed with the excitation of ultraviolet light (330–385 nm) from inset in Figure 9, which indicated the promising application of ZnS/BC nanocomposites in fluorescence materials.

## CONCLUSION

The uniform spherical ZnS nanoparticles were successfully fabricated by *in situ* homogeneous precipitation using BC as templates. We can obtain different size and distribution of ZnS nanoparticles by changing the zinc precursor concentrations. A high photocatalytic activity of ZnS/BC nanocomposites (1 wt %) with a maximum degradation efficiency (92%) of MO can be observed. The resultant ZnS/BC nanocomposites exhibited an intense blue photoluminescence at 468 nm with ultraviolet excitation (320 nm). The ZnS/BC nanocomposites integrating the excellent properties of BC and ZnS have potential application in fluorescence and photo catalysis materials.

## ACKNOWLEDGMENTS

This work was financially supported by Program of Introducing Talents of Discipline to Universities (B07024), The Fundamental Research Funds for the Central Universities, The National Natural Science Foundation of China (51273043), Project of the Action on Scientists and Engineers to Serve Enterprises (2009GJE20016), and the Fundamental Research Funds for the Central Universities (2232013D3-01).

## REFERENCES

1. Bhargava, R. N.; Gallagher, D.; Hong, X.; Nurmikko, A. *Phys. Rev. Lett.* **1994**, *72*, 416.
2. Kanemoto, M.; Shiragami, T.; Pac, C.; Yanagida, S. *J. Phys. Chem.* **1992**, *96*, 3521.
3. Murugadoss, G.; Rajamannan, B.; Ramasamy, V. *J. Lumin.* **2010**, *130*, 2032.
4. Luo, L.; Chen, H.; Zhang, L.; Xu, K. L.; Lv, Y. *Anal. Chim. Acta* **2009**, *635*, 183.
5. Hu, J.; Ren, L.; Guo, Y.; Liang, H.; Cao, A.; Wan, L.; Bai, C. *Angew. Chem. Int. Edit.* **2005**, *44*, 1269.
6. Shen, Q.; Kobayashi, J.; Diguna, L. J.; Toyoda, T. *J. Appl. Phys.* **2008**, *103*, 084304.
7. Bruchez, J., Jr.; Moronne, M.; Gin, P.; Weiss, S.; Alivisatos, A. P. *Science* **1998**, *281*, 2013.
8. Hu, W.; Chen, S.; Yang, J.; Li, Z.; Wang, H. *Carbohyd. Polym.* **2014**, *101*, 1043.
9. Velumani, S.; Ascencio, J. A. *Appl. Phys. A-Mater.* **2004**, *79*, 153.
10. Abitbol, T.; Gray, D. G. *Cellulose* **2009**, *16*, 319.
11. Abitbol, T.; Wilson, J. T.; Gray, D. G. *J. Appl. Polym. Sci.* **2011**, *119*, 803.
12. Chang, C.; Peng, J.; Zhang, L.; Pang, D. *J. Mater. Chem.* **2009**, *19*, 7771.
13. Generalova, A. N.; Sizova, S. V.; Oleinikov, V. A.; Zubov, V. P.; Artemyev, M. V.; Spernath, L.; Kamyshny, A.; Magdassi, S. *Colloid Surf. A* **2009**, *342*, 59.
14. Luna-Martinez, J. F.; Hernández-Uresti, D. B.; Reyes-Melo, M. E.; Guerrero-Salazar, C. A.; González-González, V. A.; Sepúlveda-Guzmán, S. *Carbohyd. Polym.* **2011**, *84*, 566.
15. Small, A. C.; Johnston, J. H. *Curr. Appl. Phys.* **2008**, *8*, 512.
16. Li, X.; Chen, S.; Hu, W.; Shi, S.; Shen, W.; Zhang, X.; Wang H. *Carbohyd. Polym.* **2011**, *76*, 509.
17. Zheng, Y.; Yang, J.; Zheng, W.; Wang, X.; Xiang, C.; Tang, L.; Zhang, W. *Mat. Sci. Eng. C-Mater.* **2013**, *33*, 2407.
18. Gelin, K.; Bodin, A.; Gatenholm, P.; Mihranyan, A.; Edwards, K.; Strømme, M. *Polymer* **2007**, *48*, 7623.
19. Hu, W.; Chen, S.; Yang, Z.; Liu, L.; Wang, H. *J. Phys. Chem. B.* **2011**, *115*, 8453.
20. Yan, Z.; Chen, S.; Wang, H.; Wang, B.; Jang, J. *Carbohyd. Polym.* **2008**, *74*, 659.
21. Yang, Z.; Chen, S.; Hu, W.; Yin, N.; Zhang, W.; Xiang, C.; Wang, H. *Carbohyd. Polym.* **2012**, *88*, 173.
22. Zhang, W.; Chen, S.; Hu, W.; Zhou, B.; Yang, Z.; Yin, N.; Wang, H. *Carbohyd. Polym.* **2011**, *86*, 1760.
23. Celikkaya, A.; Akinc, M. *J. Am. Ceram. Soc.* **1990**, *73*, 2360.
24. Vacassy, R.; Scholz, S. M.; Dutta, J.; Plummer, C. J. G.; Houriet, R.; Hofmann, H. *J. Am. Ceram. Soc.* **1998**, *81*, 2699.
25. Chen, S.; Zhou, B.; Hu, W.; Zhang, W.; Yin, N.; Wang, H. *Carbohyd. Polym.* **2013**, *92*, 1953.

26. Hu, W.; Chen, S.; Zhou, B.; Wang, H. *Mat. Sci. Eng. B-Solid* **2010**, *170*, 88.

27. Bredol, M.; Merikhi, J. *J. Mater. Sci.* **1998**, *33*, 471.

28. Tokoh, C.; Takabe, K.; Fujita, M.; Saiki, H. *Cellulose* **1998**, *5*, 249.

29. Kanjanamosit, N.; Muangnapoh, C.; Phisalaphong, M. *J. Appl. Polym. Sci.* **2010**, *115*, 1581.

30. Barud, H. S.; Ribeiro, C.A.; Crespi, M.S.; Martines, M. A. U.; Dexpert-Ghys, J.; Marques, R. F. C.; Messaddeq, Y.; Ribeiro, S. *J. Therm. Anal. Calorim.* **2007**, *87*, 815.

31. Dong, D.; Li, L.; Zhang, X.; Han, X.; An, H. *Chin. Phys. Lett.* **2007**, *24*, 2661.

32. Limaye, M. V.; Gokhale, S.; Acharya, S. A.; Kulkarrni, S. K. *Nanotechnology* **2008**, *19*, 415602.